

Site substitution in GdMnO₃: Effects on structural, electronic, and magnetic propertiesSudipta Mahana ^{1,2,*}, Shishir Kumar Pandey,³ Bipul Rakshit,⁴ Pronoy Nandi,^{1,2} Raktima Basu,⁵ Sandip Dhara ⁵, S. Turchini,⁶ N. Zema,⁶ U. Manju,⁷ Subhendra D. Mahanti,⁸ and D. Topwal ^{1,2,†}¹*Institute of Physics, Sachivalaya Marg, Bhubaneswar 751005, India*²*Homi Bhabha National Institute, Training School Complex, Anushakti Nagar, Mumbai 400085, India*³*International Center for Quantum Materials, School of Physics, Peking University, Beijing 100871, China*⁴*Center for Superfunctional Materials, Ulsan National Institute of Science and Technology, Ulsan 44919, South Korea*⁵*Surface and Nanoscience Division, Indira Gandhi Centre for Atomic Research, HBNI, Kalpakkam 603102, India*⁶*Istituto Struttura della Materia-CNR (ISM-CNR), Roma 00133, Italy*⁷*CSIR -Institute of Minerals and Materials Technology, Bhubaneswar 751013, India*⁸*Department of Physics and Astronomy, Michigan State University, East Lansing, Michigan 48824, USA*

(Received 7 April 2020; accepted 1 December 2020; published 15 December 2020)

We report on detailed structural, electronic, and magnetic studies of GdMn_{1-x}Cr_xO₃ for Cr doping levels; $x = 0 \leq x \leq 1$. X-ray diffraction studies suggest that GdMn_{0.5}Cr_{0.5}O₃ has a monoclinic $P2_1/b$ structure with alternate arrangements of Mn and Cr atoms along the [001] direction. In the solid solutions, the Jahn-Teller distortion associated with Mn³⁺ ions gives rise to major changes in the bc -plane sublattice and also an effective orbital ordering in the ab plane, which persist up to compositions $x \sim 0.35$. These distinct features in the lattice and orbital degrees of freedom are also correlated with bc -plane anisotropy of the local Gd environment. A gradual evolution of electronic states with doping is also clearly seen in O K -edge x-ray absorption spectra. Evidence of magnetization reversal in field-cooled-cooling mode for $x \geq 0.35$ coinciding with the Jahn-Teller crossover suggests a close correlation between magnetic interaction and structural distortion. These observations indicate a strong entanglement between lattice, spin, electronic, and orbital degrees of freedom. The nonmonotonic variation of remnant magnetization can be explained by doping-induced modification of magnetic interactions. Density-functional-theory calculations are consistent with layer-by-layer-type arrangements of Cr ions and Mn ions with ferromagnetic (antiferromagnetic) coupling between Mn (Cr) ions for intermediate compounds ($x = 0.5$). For $x = 0.25$ compositions, we found alternate layers of Mn and mixed Mn-Cr atoms stacked along the c axis with intralayer ferromagnetic coupling and interlayer antiferromagnetic coupling. For $x = 0.75$ compositions, there exists strong antiferromagnetic coupling between half-filled t_{2g} orbitals of in-plane Cr ions along with a ferromagnetic Mn-Cr coupling.

DOI: [10.1103/PhysRevB.102.245120](https://doi.org/10.1103/PhysRevB.102.245120)**I. INTRODUCTION**

Functional oxides with perovskite structures (ABO_3) are a very active research area not only due to their potential technological applications but also for their fundamental importance in basic scientific research. An unusual aspect of perovskites is their ability to incorporate almost every element of the periodic table at the A and B sites due to their capacity to accommodate various structural distortions [1]. External parameters like temperature, pressure, and chemical compositions can also drive such distortions, which leads to an extraordinary richness of physical properties within the family of perovskites. Structural distortions in perovskites are mainly associated with three main features with respect to their ideal cubic structure [1–3]: (i) rotation (tilt) of BO_6 octahedra, (ii) polar cation dis-

placements, which often lead to ferroelectricity, and (iii) distortions of the octahedra, such as the Jahn-Teller (JT) distortion.

Rare-earth manganites ($RMnO_3$) invoked great interest owing to the JT character of Mn³⁺ ions ($t_{2g}^3 e_g^1$), exhibiting orbital ordering along with highly anisotropic Mn–O bond lengths [4]. A complex interplay among the spin, orbital and lattice degrees of freedom has led to a large number of intriguing physical properties in both pristine and doped $RMnO_3$ such as colossal magnetoresistance [5], charge and orbital ordering [6–8], metal-insulator transition [9,10], complex spin structures [11], and multiferroic properties with significant magnetoelectric coupling [12]. In contrast to Mn³⁺, Cr³⁺ is a JT inactive ion because of having completely empty e_g orbitals and therefore the oxygen octahedra are more regular. However, most of the members of $RCrO_3$ have been reported to be multiferroic materials at considerable high temperature [13,14]. Additionally, $RCrO_3$ systems are of great interest as these exhibit complex magnetic properties such as spin-reorientation (SR), spin-flipping (SF), and temperature-induced magnetization reversal (TMR), etc. [15–17].

*Present address: Rajdhani College, Baramunda Square, Nayapalli, Bhubaneswar 751003, Odisha, India.

†dinesh.topwal@gmail.com

GdMnO₃ with the orthorhombic *Pbnm* structure exhibits incommensurate sinusoidal magnetic ordering arising from competing nearest-neighbor ferromagnetic (NN-FM) and next-nearest-neighbor antiferromagnetic (NNN-AFM) interaction followed by a canted-A-type ordering in the Mn sublattice [11,18]. Additionally, a low-temperature ferroelectric ordering is established, caused by Gd³⁺-Mn³⁺ spin interactions and/or lattice distortions associated with magnetic field-induced spin rearrangements [19,20]. GdCrO₃ is one of the *G*-type antiferromagnetic (AFM) RCrO₃ compounds, exhibiting extremely rich magnetic properties like TMR, SF, SR, and others [15]. It has a noncentrosymmetric *Pna2*₁ structure associated with the ferroelectric transition concurrent to Cr magnetic-ordering temperature with significant magnetoelectric coupling [13,14]. Although the parent compounds without doping are well investigated, the solid solution GdMn_{1-x}Cr_xO₃ is largely unexplored [21]. Various interesting properties have been reported in similar types of mixed cation compositions such as DyMn_{1-x}Fe_xO₃ [22], LaMn_{1-x}Fe_xO₃ [23], TbMn_{1-x}Fe_xO₃ [24], YbMn_{1-x}Fe_xO₃ [25], TbMn_{1-x}Cr_xO₃ [26], and others. This has motivated us to investigate the GdMn_{1-x}Cr_xO₃ series.

In this paper, we present systematic structural, electronic, and magnetic investigations of the solid solutions, GdMn_{1-x}Cr_xO₃ ($0 \leq x \leq 1$). Substitution of the Mn ions in GdMnO₃ by Cr ions gives rise to local distortions around the Cr ion, resulting in average lattice distortions in the compound. However, at considerable Cr concentration, the JT-induced distortions are negligible, resulting in a crossover from a JT active region to JT inactive region.

II. EXPERIMENTAL AND THEORETICAL DETAILS

Polycrystalline samples of Cr-doped gadolinium manganites, GdMn_{1-x}Cr_xO₃ ($0 \leq x \leq 1$) were prepared by the solid-state synthesis technique as reported elsewhere [18]. The crystalline structure and phase purity of the solid solutions were confirmed by x-ray diffraction (XRD) measurements using a Bruker D8 Advance x-ray diffractometer equipped with Cu *K*_α radiation. Rietveld refinements of the obtained powder XRD patterns were carried out using the FULLPROF program. Raman spectroscopy measurements were performed using a micro-Raman spectrometer (inVia, Renishaw, United Kingdom) with 514.5 nm excitation of an Ar⁺ laser. Spectra were collected in the backscattering configuration using a thermoelectrically cooled CCD camera as the detector and a long working distance 50× objective with a numerical aperture of 0.45 used for the acquisition. Magnetization measurements were carried out in Quantum Design Physical Property Measurement System equipped with a vibrating sample magnetometer. The O *K*-edge x-ray absorption spectra were recorded in total electron yield mode at the circular polarization beamline at the Elettra synchrotron radiation facility.

Our theoretical calculations of the structural, electronic, and magnetic properties were based on density-functional theory, using generalized gradient approximation (GGA) with Perdew-Burke-Ernzerhof for solids [27] parametrization for the exchange correlation potential, the projector augmented-wave (PAW) method [28], and a plane-wave basis set, as

implemented in the VIENNA AB INITIO SIMULATION PACKAGE [29]. The interaction between ions and electrons was approximated with PAW potentials, treating 3*p*, 3*d*, and 4*s* for Cr/Mn and 2*s* and 2*p* for O as valence electrons. For Brillouin zone sampling, we chose 12 × 12 × 8 Monkhorst-Pack *k*-point mesh [30] and the wave function was expanded in a basis set consisting of plane waves with kinetic energies less than or equal to 770 eV. Using these parameters, an energy convergence of less than 1 meV/formula unit (f.u.) was achieved. Structures were fully relaxed until residual Hellmann-Feynman forces were smaller than 0.001 eV/Å while maintaining the symmetry constraints of the given space group. Gd 4*f* electrons were treated as valence electrons for the parent compounds. We performed calculations using different Hubbard *U* values up to 4 eV for Mn/Cr and 4 eV for Gd and results for *U* = 3 eV for Mn/Cr and 4 eV for Gd explain satisfactorily the x-ray absorption spectra, which will be discussed in a later section. In GdMn_{0.5}Cr_{0.5}O₃, Gd 4*f* electrons were treated as core electrons to reduce the calculations time. Irrespective of the two models, the 4*f* states lie deep in energy and they are almost completely localized so they do not affect in any essential way other valence states [31]. To visualize the orbital ordering in GdMnO₃, in addition to the global *X*, *Y*, *Z* orthorhombic frame, a local frame specific to each JT-type distorted MnO₆ octahedron was defined choosing *x*, *y*, *z* along the middle, short, and long Mn-O axes, respectively [31].

III. RESULTS AND DISCUSSION

Figure 1(a) depicts room temperature XRD patterns of the solid solutions GdMn_{1-x}Cr_xO₃ ($0 \leq x \leq 1$) along with the corresponding Rietveld refined patterns. $x = 0, 0.25$, and 0.75 compositions are fitted with *Pbnm* space group, whereas $x = 0.5$ composition is fitted with *P2*₁/*b* space group and $x = 1.0$ composition is fitted with *Pna2*₁ space group. GdMn_{0.5}Cr_{0.5}O₃ is also fitted well with the *Pbnm* space group having reliability parameters $R_{wp} \sim 0.112$, $R_{exp} \sim 0.069$, and $\chi^2 \sim 3.21$ (see Fig. S1 in the Supplemental Material [32]). However, if we look carefully at the XRD data, there is a very weak peak present slightly below 30°, which is most likely a supercell peak. Therefore, we tried to fit the data with possible *B*-site ordered structure (rock salt *P2*₁/*c* and monoclinic *P2*₁/*b*). Surprisingly, we find that the *P2*₁/*b* space group also fits well and the reliability parameters are quite similar to that of *Pbnm* space group ($R_{wp} \sim 0.14$, $R_{exp} \sim 0.056$, and $\chi^2 \sim 3.43$). In a monoclinic structure with *P2*₁/*b* space group, Mn and Cr atoms occupy 2*b* (0, 0, 0.5) and 2*a* (0, 0, 0) sites, respectively, whereas in the *Pbnm* structure Mn and Cr atoms are randomly arranged [33]. The reason for good fitting of both ordered and disordered structures is possibly due to the similar ionic radii and atomic form factors of Mn³⁺ and Cr³⁺ ions, and XRD is not sensitive enough to distinguish them. Moreover, in the refinement with *P2*₁/*b* structure, the calculated (102)-diffraction position does correspond to the weak peak present slightly below 30°, whereas it is absent in the calculated XRD patterns by using the *Pbnm* structure. Therefore, it seems that the *B*-site ordered *P2*₁/*b* space group is more reasonable in GdMn_{0.5}Cr_{0.5}O₃ rather than the *B*-site

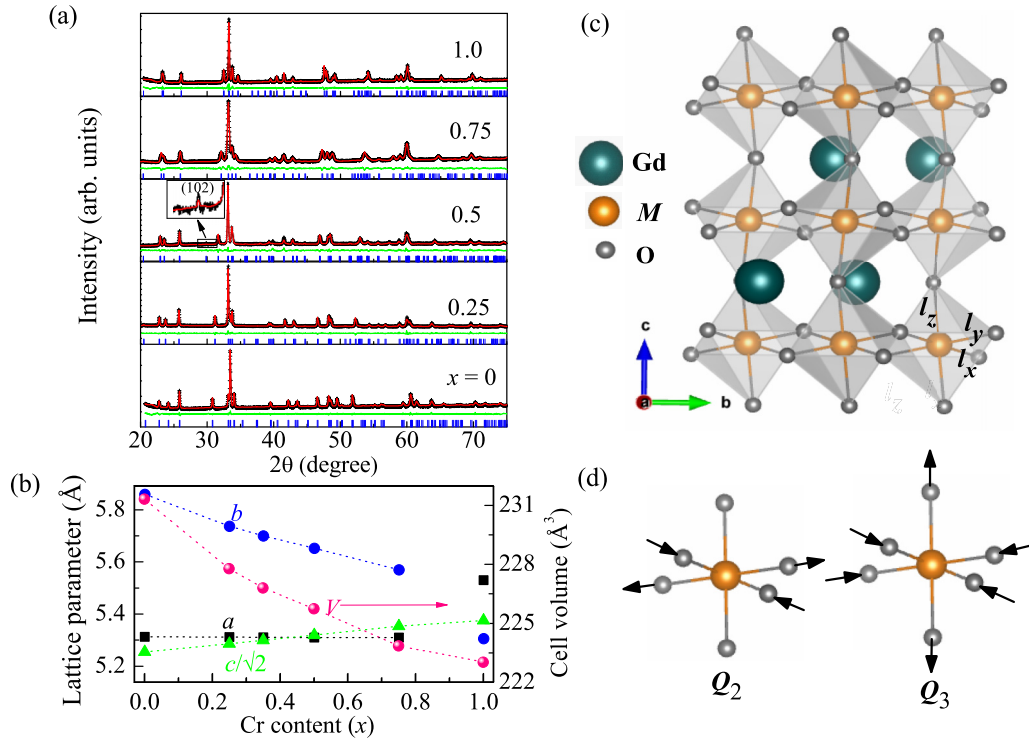


FIG. 1. (a) The Rietveld-refinement plots of room temperature XRD patterns of GdMn_{1-x}Cr_xO₃ ($x = 0, 0.25, 0.5, 0.75, \text{ and } 1.0$). $x = 0, 0.25, \text{ and } 0.75$ compositions are fitted with $Pbnm$ space group, whereas $x = 0.5$ composition is fitted with $P2_1/b$ space group and $x = 1.0$ composition is fitted with $Pna2_1$ space group. Experimental data is presented with symbols while the fitted curves from the Rietveld analysis are represented as red lines. Difference spectra (difference between experimental data and fitting) is plotted in green lines. Blue vertical lines represent Bragg positions. Inset shows enlarged view of superlattice peak (102) of GdMn_{0.5}Cr_{0.5}O₃ for $P2_1/b$ structure. (b) Evolution of the cell parameters (a , b , and, $c/\sqrt{2}$ (left panel) and cell volume (V) (right panel) as a function of compositions (x). As GdCrO₃ has $pn2_1$ symmetry, lattice parameters a and b interchange with respect to other compositions having $Pbnm$ symmetry. (c) Crystal structure of GdMO₃. (d) Normal modes of distortion; Q_2 (orthorhombiclike distortion) and Q_3 (tetragonal-like distortion), respectively.

disordered $Pbnm$ structure. The $Pna2_1$ space group is considered to fit GdCrO₃ as reported earlier [14].

The composition-dependent evolution of the lattice parameters (a , b , and $c/\sqrt{2}$) and the cell volume (V) in GdMn_{1-x}Cr_xO₃ are shown in Fig. 1(b). A remarkable decrease in the value of the b axis accompanied with an increase of the c axis value has been observed with increasing Cr content, while the a axis remains almost constant. This suggests that lattice degrees of freedom confined to the bc plane are strongly affected by the substitution of Cr. Further, the decrease in the cell volume reveals that the c -axis elongation is smaller than the b -axis reduction. Such structural characteristics cannot be understood by considering the ionic radii of Cr³⁺ ions (0.615 Å) in place of Mn³⁺ ions (0.645 Å) alone.

To understand the physics of structural changes when Cr³⁺ ions replace Mn³⁺ ions, a detailed Rietveld refinement of the XRD patterns was carried out and the composition-dependent variations of three M -O bonds ($M = \text{Mn/Cr}$) in the MO_6 octahedra are shown in Fig. 2(a), with l_x , l_y , and l_z denoting bond lengths along the respective local axes discussed in the experimental details. The intrinsic octahedral distortion in the orthorhombic structure allows the short and long bonds to lie within the ab plane and the intermediate bond length along the c axis [22,34]. The large differences among the three M -O bond lengths in GdMnO₃ are correlated with the JT distortion of Mn³⁺ ions along with a contribution from

intrinsic structural distortion. In contrast, GdCrO₃ exhibits a regular structure with similar bond lengths of l_x , l_y , and l_z , consistent with the absence of JT distortion for the Cr³⁺ ions. The local parameters characterizing the JT distortion are defined as in- (ab) plane orthorhombic distortion, $Q_2 [= l_y - l_x]$ and out-of-plane (along c axis) tetragonal-like distortion, $Q_3 [= (2l_z - l_x - l_y)/\sqrt{3}]$ [Fig. 1(d)] [22,35,36]. The composition-dependent variations of Q_2 and Q_3 are shown in Fig. 2(b). The large positive value of Q_2 in GdMnO₃ is associated with the cooperative JT distortion, which is along the b axis and Q_3 with negative sign indicates that an out-of-plane distortion along the c axis is competing with the JT distortion [22,35]. This implies that the lattice deformation is primarily confined to the bc plane. Q_2 remains at a higher value than Q_3 up to the compositions $x \sim 0.35$, corroborating ab -plane distortion is predominant in these compositions. In addition, it indicates that the increase of the c axis is largely overwhelmed by decrease of the b axis. Upon approaching toward GdCrO₃, the decrease of both Q_2 and Q_3 indeed reveals a gradual decrease of both orthorhombic and tetragonal distortions. An intriguing slope change in both Q_2 and Q_3 around $x \sim 0.35$ (guided by the dotted lines in Q_2) indicates the suppression of long-range structural distortion associated with local JT distortion at the Mn sites.

Further examination of the average octahedral distortion $\Delta_d [= (1/6) \sum_{n=1-6} [(d_n - \langle d \rangle) / \langle d \rangle]^2]$, where d_n ($\langle d \rangle$) is the

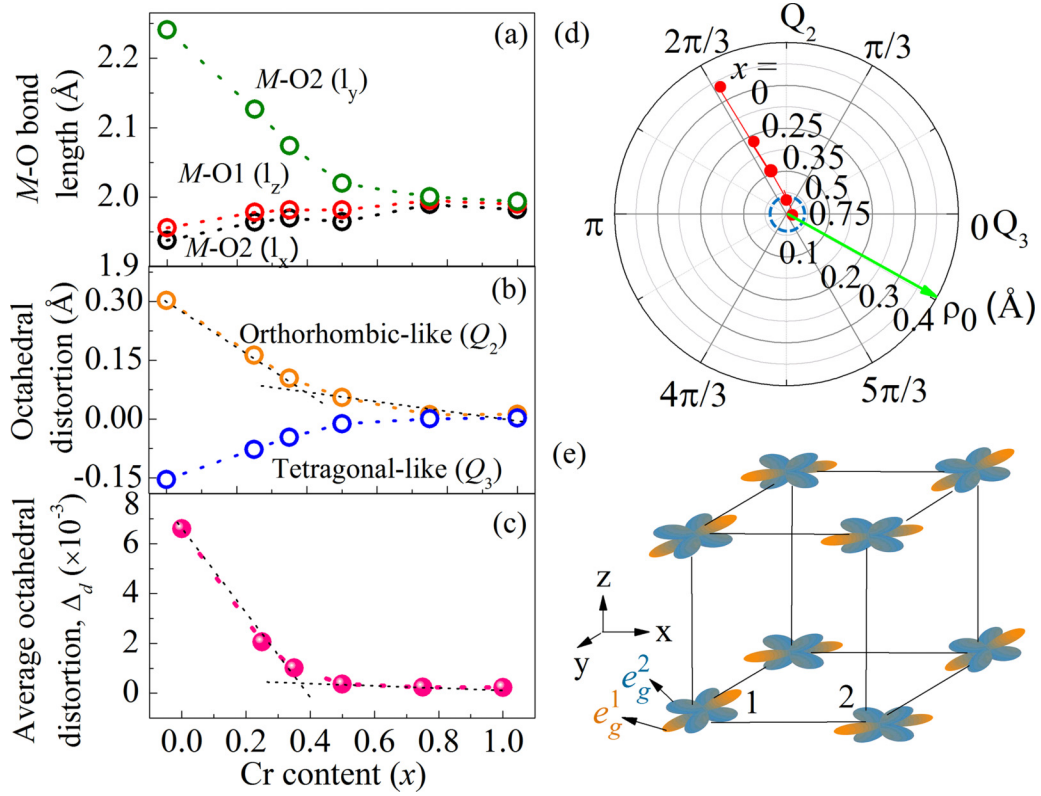


FIG. 2. (a) The composition-dependent variations of the M -O bonds in the MO_6 octahedra of $GdMn_{1-x}Cr_xO_3$, with the long, short M -O2 bonds and the middle M -O1 bond, respectively. O1 (O2) represents the apical (equatorial) oxygen along the c axis. For $x = 0.5$ composition, the average bond lengths of distinct Mn-O and Cr-O bonds along respective axes are plotted as having $P2_1/b$ symmetry. (b) The composition-dependent variations of in- (ab) -plane orthorhombiclike (Q_2) and out-of-plane tetragonal-like (Q_3) distortions. Dotted line guiding Q_2 point to the slope crossover around $x \sim 0.35$. (c) Variation of average octahedral distortion evaluated by Δ_d . Dotted lines guiding Δ_d to the slope crossover as a result of effective suppression of JT orbital ordering around $x \sim 0.35$. All the parameters are derived from the Rietveld refinements of the respective XRD patterns. (d) The polar plot of ρ_0 ($= \sqrt{Q_2^2 + Q_3^2}$) and ϕ ($= \tan^{-1}(Q_3/Q_2)$), which are used to describe the orbital mixing in $GdMn_{1-x}Cr_xO_3$. (e) Schematic diagram of e_g orbitals of Mn^{3+} due to the JT orbital ordering.

individual (average) M -O bond length] [depicted in Fig. 2(c)], shows a slope changeover around $x \sim 0.35$ (guided by the dotted lines), a characteristic of crossover from the JT-dominated region to the JT-inactive region (on the average).

The JT effect results in the lifting of degeneracy of e_g orbitals of Mn^{3+} ions and is responsible for building up orbital ordering in the material. Thus, there is a correlation between JT distortion and ab -plane staggered orbital ordering. A polar plot of magnitude of the octahedral-site distortion, ρ_0 ($= \sqrt{Q_2^2 + Q_3^2}$) versus the angle ϕ ($= \tan^{-1}(Q_3/Q_2)$), was mapped for the compositions as shown in Fig. 2(d), where ϕ is measured from the Q_2 axis in an anticlockwise direction [37].

The description of the e_g orbital associated with the M atom in an MO_6 octahedron can be made by the wave function ψ with a linear combination of orbitals $|x^2 - y^2\rangle$ and $|3z^2 - r^2\rangle$ in the (Q_2 , Q_3) space as given by [4,38]

$$\psi(\theta) = \cos(\theta/2) |3z^2 - r^2\rangle + \sin(\theta/2) |x^2 - y^2\rangle,$$

where the angle θ ($\theta = 90^\circ + |\phi|$) represents respective orbital components, which is measured in an anticlockwise direction from the Q_3 axis. $\theta = 0, 2\pi/3$, and $4\pi/3$ correspond to orbitals $|3z^2 - r^2\rangle$, $|3y^2 - r^2\rangle$, and $|3x^2 - r^2\rangle$, respectively, and $\theta = \pi/3, \pi$ and $5\pi/3$ represent $|y^2 - z^2\rangle$, $|x^2 - y^2\rangle$ and

$|z^2 - x^2\rangle$, respectively. An octahedral site distortion, which has a θ deviating from these special angles reflects either the presence of orthorhombic distortion or a combination of orbital ordering and orthorhombic distortion. Figure 3(b) depicts the schematic representation of orbital ordering in Mn^{3+} ions in $GdMnO_3$. Since for all compositions in $GdMn_{1-x}Cr_xO_3$, θ falls between the special angle and close to $2\pi/3$ for one of the coplaner Mn-sites (site 1) as defined in Fig. 2(e) (it is close to $4\pi/3$ for site 2), a new angle $\gamma = \pi/6 - \phi$ can be defined to simplify the wave functions for occupied (e_g^1) and unoccupied (e_g^2) orbitals for site 1, such that [4,38]

$$\begin{aligned} \psi_{\text{occ}}(\gamma) &= \cos(\gamma/2) |3y^2 - r^2\rangle + \sin(\gamma/2) |z^2 - x^2\rangle, \\ \psi_{\text{unocc}}(\gamma) &= -\sin(\gamma/2) |3y^2 - r^2\rangle + \cos(\gamma/2) |z^2 - x^2\rangle. \end{aligned}$$

The total site distortion, as measured by ρ_0 , remains above 0.3 up to $x \sim 0.35$ compositions, reflecting a dominant contribution from a static JT orbital mixing along with the octahedral distortion [4,38]. For $x = 0.5$ and higher compositions, ρ_0 is about one order of magnitude smaller than that of JT-active $GdMnO_3$ and other manganites ($RMnO_3$) and resembles the one found in JT-inactive rare-earth ferrites ($RFeO_3$) and vanadites (RVO_3), indicating the disappearance of orbital ordering [4,35,38].

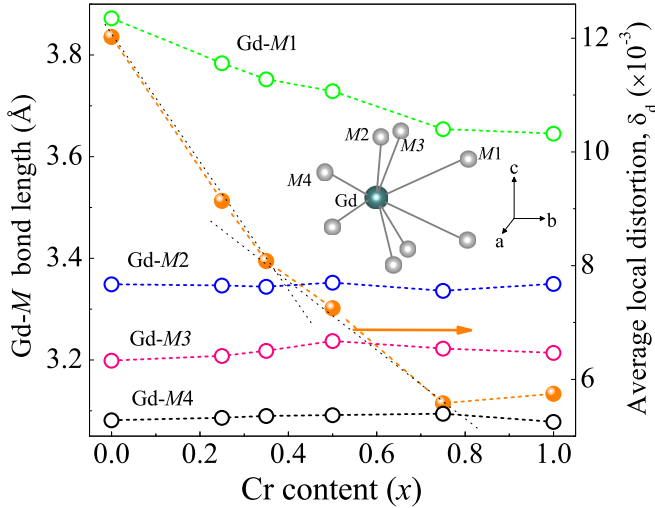


FIG. 3. The evolution of the lattice anisotropy specific to the local Gd environment through variations in the nearest-neighbor Gd- M bond lengths. Right panel represents corresponding average local distortion (δ_d) in the local Gd- M environment. Dotted lines guiding δ_d signify the slope crossover around $x \sim 0.35$. Inset represents nearest-neighbor Gd- M bond lengths with blue atom, Gd, and gray atoms, M . All the parameters are derived from the Rietveld refinements of the respective XRD patterns.

To examine lattice anisotropy specific to the local Gd environment, NN Gd- M bond lengths are plotted, as shown in Fig. 4. There are eight NN-coordinated M which are doubly paired as $M1$ - $M4$, as viewed schematically in the inset of Fig. 3. Each pair of Gd- M lengths are equivalent for all compositions except GdCrO₃, in which they are unequal (slightly) due to the $Pna2_1$ symmetry. The longest Gd- $M1$ (shortest Gd- $M4$) lying in the bc plane shows a visible reduction (slight increase) toward $x = 1$, which is due to the suppression of JT distortion predominantly along the b axis. The corresponding average local distortion, $\delta_d [= (1/8) \sum_{n=1-8} [(d_n - \langle d \rangle) / \langle d \rangle]^2]$, where d_n ($\langle d \rangle$) is the individual (average) Gd- M bond length] also shows a decrease of local anisotropy with an increase of Cr content followed by a slight increase in GdCrO₃ owing to having $Pna2_1$ symmetry. A slope change occurs (guided by dotted line) around the critical concentration, $x \sim 0.35$ of JT crossover, consistent with earlier discussions. This suggests that the evolution of lattice and orbital degrees freedom in the solid solutions is also correlated with the bc -plane anisotropy in the local Gd environment [22].

To understand the lattice/atomic vibrations present in the above system and their role in the structural deformations, room-temperature Raman spectroscopy measurements were performed in the solid solutions, as depicted in Fig. 4. According to group theoretical calculations, orthorhombic $Pbnm$ structure has 24 Raman-active modes ($7A_g + 7B_{1g} + 5B_{2g} + 5B_{3g}$) at the Γ point of the Brillouin zone [14,39,40]. The Raman modes in RMO_3 orthorhombic perovskites are activated by only one of four basic distortions such as rotation of MO_6 octahedra around $[001]_C$ and $[110]_C$ axes, JT-like distortion, and R shifts from its position in an ideal perovskite lattice and the relative intensity of Raman peaks depends on the different magnitude of these four basic distortions [41,42].

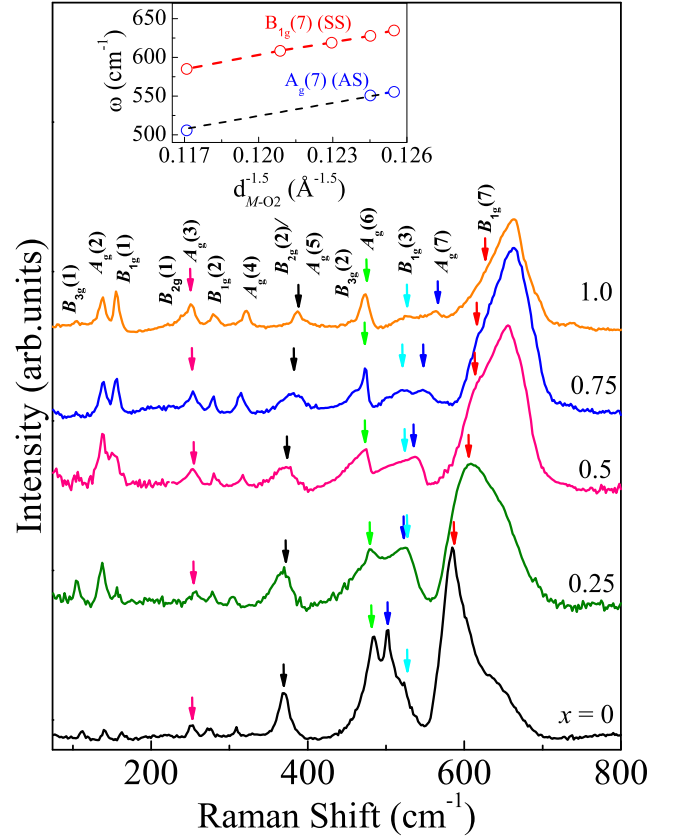


FIG. 4. (a) Evolution of room-temperature Raman spectra with compositions (x) in GdMn_{1-x}Cr_xO₃ ($x = 0, 0.25, 0.5, 0.75$, and 1.0). The inset shows the linear dependence of the JT symmetric stretching [$B_{2g}(7)$] and antisymmetric stretching [$A_g(7)$] mode frequency with the $d_{M-O_2}^{-1.5}$, where d_{M-O_2} is the average of short and long $M-O_2$ bond lengths. $A_g(7)$ mode for $x = 0.25$ and 0.5 compositions are not shown, as it is not possible to determine their positions accurately due to the asymmetric shape of peaks and the presence of the neighboring $B_{1g}(3)$.

Therefore, depending on the magnitude of basic distortions in the system, some peaks are either weak or invisible as evidenced in LaCrO₃ and CaMnO₃ from lattice dynamical calculations [41,42]. Further, some of the Raman bands exhibit strong resonant behavior on the excitation wavelength as reported in LaCrO₃ and CaMnO₃ [41,42]. It is observed that intensity of some peaks increases with increase of excitation wavelength and of other peaks decreases, and it is concluded that 515 nm is a suitable wavelength for Raman measurements for simultaneous observation of all peaks. We have done measurements with 514.5-nm excitation wavelength, very close to 515 nm and found 14 Raman modes which are consistent with the literature on both single crystals and polycrystals of GdMnO₃ and GdCrO₃ [14,39,40]. Therefore, it seems that the other predicted modes are either too low in intensity or beyond our experimental range to be observed. The details about the observed modes are described elsewhere [14,26,39,40]. The modes around 670 cm⁻¹ may be the disorder-induced phonon density of states (DOS) of oxygen vibrations [43,44]. Apart from this, Kovaleva *et al.* argued that there is an additional component to the multiorder scattering, which may arise from

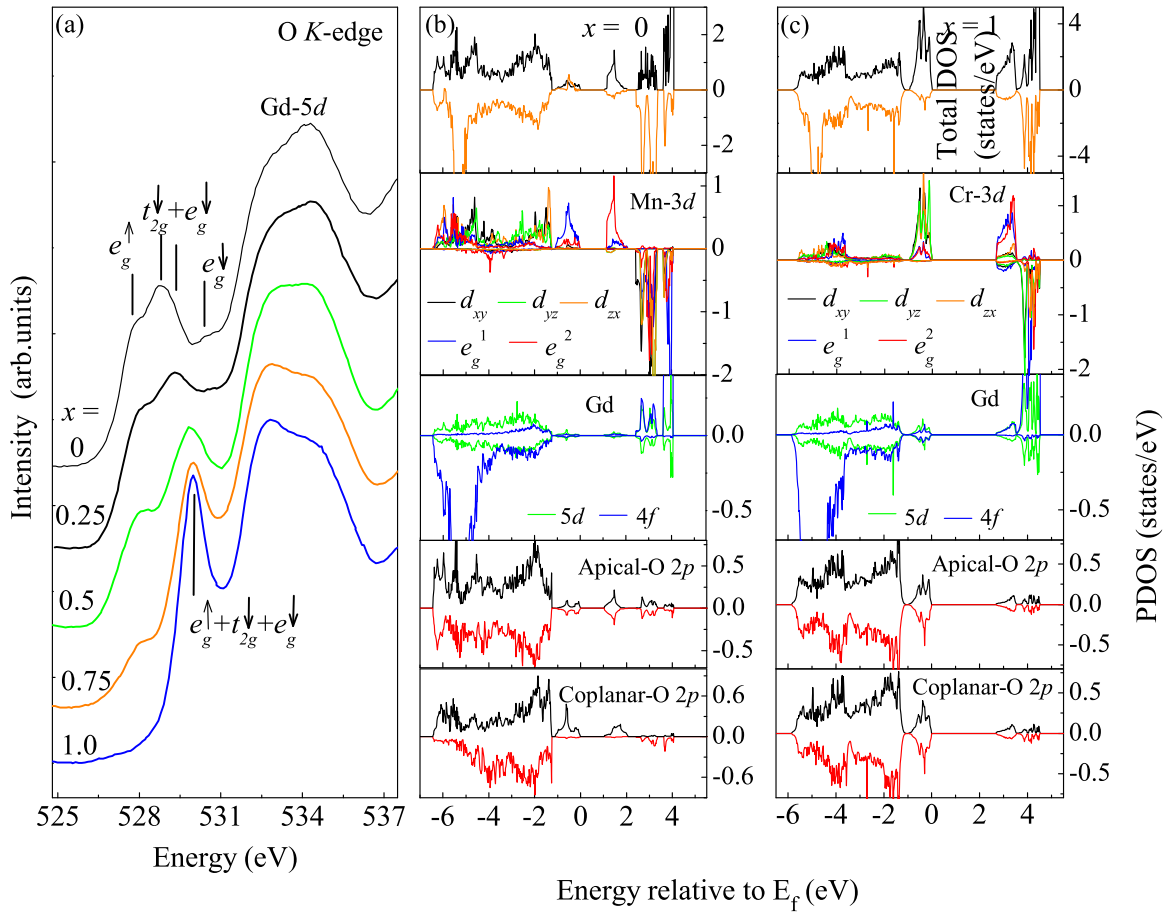


FIG. 5. (a) Evolution of O K -edge XAS spectra with compositions (x) in $\text{GdMn}_{1-x}\text{Cr}_x\text{O}_3$ ($x = 0, 0.25, 0.5, 0.75$, and 1.0). (b), (c) The total and site-decomposed DOS of GdMnO_3 and GdCrO_3 , respectively.

coupling between the low-energy electronic excitations and the vibrational modes [45].

The most common distortion in orthorhombic $Pbnm$ structure is the tilting of BO_6 octahedra, which can be described either by orthogonal tilt angles (leading to the $a^-a^-c^+$ Glazer's notation) or by octahedral tilts θ , ϕ , and Φ around the pseudocubic $[110]_{\text{pc}}$ and $[001]_{\text{pc}}$, and $[111]_{\text{pc}}$ axes [3,46–48]. The Raman modes $A_g(3)$ and $A_g(5)$ are correlated with the tilt angles ϕ and θ , respectively [39,47]. The position of $A_g(3)$ remains unchanged throughout the series, i.e., ϕ remains constant. In contrast, $A_g(5)$ shows hardly any shift up to $x \sim 0.5$ compositions and, thereafter, it shifts around 15 cm^{-1} toward high frequency for $x = 0.75$ and 1.0 compositions. This, in turn, suggests that θ remains more or less constant up to $x \sim 0.5$ compositions and slightly increases (negligibly small) for $x = 0.75$ and 1.0 compositions. Furthermore, Φ is correlated with θ and ϕ via the relation, $\cos\Phi = \cos\theta \cos\phi$ [46,47], implying that Φ also increases slightly for $x = 0.75$ and 1.0 compositions. The in-plane antisymmetric stretching [$A_g(7)$] and symmetric stretching [$B_{1g}(7)$] modes are the JT modes, which are associated with the M -O2 bond lengths in ab planes. The variation of frequency of these modes follows the relation, $\omega \propto d_{M-O2}^{-1.5}$ [39,49], as shown in the inset of Fig. 4. $A_g(7)$ and $B_{1g}(7)$ modes show a clear shift up to $x \sim 0.5$ compositions. Previously parameters extracted from the

XRD patterns, depicted in Fig. 2, shows a rapid decrease of M -O2 bond lengths with Cr doping up to $x \sim 0.5$, suggesting that the clear shift in modes are arising from the rapid decrease of M -O2 bond lengths. Beyond $x \sim 0.5$ compositions, both the variation in M -O2 bond lengths as well as the shift in modes become lesser, suggesting strong interdependence. With Cr doping, there is a rapid decrease of M -O2 bond lengths up to $x \sim 0.5$ (Fig. 2), leading to a clear shift of these two modes after that shift is less. Furthermore, the spectral weight also decreases dramatically with increase of Cr content (x) due to the reduction of JT distortion and becomes weak for .75 and 1.0 compositions, which are JT-inactive compounds.

X-ray absorption spectroscopy (XAS) measurements were performed at the O K -edge of the solid solutions for $x = 0, 0.25, 0.5, 0.75$, and 1 to obtain information about the unoccupied M 3d, Gd 5d and deep Gd/ M states via the hybridization with the O 2p states [22,50], see Fig. 5(a). To understand XAS features, we performed DOS calculations on the end compositions; GdMnO_3 ($x = 0$) and GdCrO_3 ($x = 1$) as shown in Figs. 5(b) and 5(c), respectively. Due to JT orbital ordering, the e_g^{\uparrow} band splits into two subbands: occupied e_g^{\uparrow} mainly dominated by $|3y^2 - r^2\rangle$ with a small contribution from $|z^2 - x^2\rangle$ and unoccupied e_g^{\downarrow} , mainly contributed by $|z^2 - x^2\rangle$ mixing with $|3y^2 - r^2\rangle$ for one of the co-planar Mn

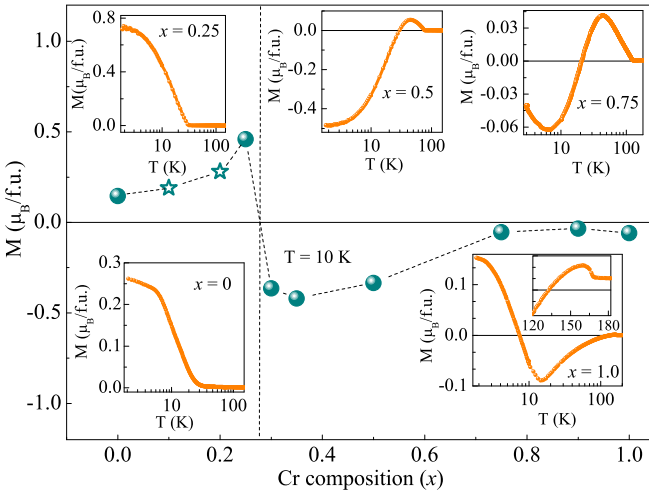


FIG. 6. Variation in magnetic moment at 10 K with compositions (x) in $\text{GdMn}_{1-x}\text{Cr}_x\text{O}_3$. Stars (*) represent the results extracted from Ref. [21]. Insets represent temperature-dependent magnetization measured in field-cooled-cooling protocol of the solid solutions for $x = 0, 0.25, 0.5, 0.75$, and 1.

sites (for other co-planar Mn sites, these two e_g orbitals are a mixture of $|3x^2 - r^2\rangle$ and $|y^2 - z^2\rangle$), as discussed earlier. Based on DOS calculations, it can be argued that the features between 526.5–531 eV in the O K -edge spectra of GdMnO_3 are contributed by unoccupied $e_g \uparrow$ ($e_g^2 \uparrow$), $t_{2g} \downarrow + e_g \downarrow$ and $e_g \downarrow$ [22,50,51], as labeled in Fig. 5(a). The first peak around 527.8 eV arises from $e_g^2 \uparrow$ states. From the partial DOS [Fig. 6(b)], a gap of 1.2 eV is obtained between these JT-split Mn $e_g \uparrow$ bands, which is in agreement with the calculated indirect band gap from absorption study of polycrystalline GdMnO_3 [52]. The second peak of XAS spectrum around 529 eV is associated with $t_{2g} \downarrow$ and $e_g \downarrow$ states, with a small contribution from $e_g \downarrow$ around 530.5 eV. Furthermore, there is a splitting of 1.4 eV between $e_g^2 \uparrow$, $t_{2g} \downarrow + e_g \downarrow$ states, which agrees satisfactorily with our calculations. In contrast to GdMnO_3 , the O K -edge for the JT-inactive GdCrO_3 shows a single peak between 529–531 eV contributed by all unoccupied states of Cr^{3+} , i.e., $e_g \uparrow$, $t_{2g} \downarrow$ and $e_g \downarrow$ states and is in good agreement with the calculated PDOS [Fig. 5(c)]. The energy gap of 2.7 eV obtained from the calculation agrees well with the experimentally obtained band gap values reported in chromite family [53,54]. The above studies suggest that the first hump (527.8 eV) in XAS spectra for intermediate compositions generally arise from contribution of the $e_g^2 \uparrow$ state of Mn atoms and a second broad hump contributes from the $e_g \uparrow$ state of Cr and $t_{2g} \downarrow$ and $e_g \downarrow$ state of both Mn and Cr ions. A gradual decrease of the first peak with increasing Cr composition is clearly observed.

The broad feature between 531–537 eV [Fig. 5(a)] corresponds to Gd $5d$ states, indicating hybridization of Gd $5d$ and M $3d$ ($e_g \uparrow$) states mediated through oxygen, suggesting Gd($4f$)- M ($3d$) electronic coupling in these compounds [55,56]. Due to the highly localized character of the $4f$ states, direct $3d(M)$ - $4f(\text{Gd})$ coupling is unlikely. Hence the interactions occur via $5d$ states as they are partially polarized by the $4f$ electrons via intra-atomic $4f$ - $5d$ exchange interaction. The

spin polarized $5d$ states couple with M - $3d$ states either directly or indirectly through O- $2p$ states [55,56]. The $3d$ - $4f$ interactions via hybridized $5d$ and O- $2p$ states is also evidenced from the calculated DOS of GdMnO_3 and GdCrO_3 [Figs. 5(b) and 5(c)].

Temperature-dependent magnetization measurements were performed on the solid solutions, $\text{GdMn}_{1-x}\text{Cr}_x\text{O}_3$, for $0 \leq x \leq 1$. Figure 6 depicts variations in magnetic moment at 10 K with doping concentration and insets represent temperature-dependent magnetization measured in field-cooled-cooling (FCC) mode for various x values as indicated. Due to the cooperative JT orbital ordering in GdMnO_3 , NNN-AFM coupling plays a significant role in addition to NN-FM coupling in the ab plane. In addition, there exists an AFM coupling between these layers along the c axis. The competition between these leads to sinusoidal ordering below 40 K followed by canted A -type ($A_y F_z$ in Bertaut's notation) ordering below 20 K in Mn sublattices as described in detail in our earlier report [18]. Remarkably, magnetization at low temperature (10 K) increases gradually upon Cr doping up to $x \sim 0.25$ in spite of the fact that Cr^{3+} moment is smaller than the Mn^{3+} moment, indicating the strengthening of ferromagnetic (FM) interactions (or weakening of the AFM interaction) in the system. This is probably due to the increase in the strength of NN-FM coupling as compared to NNN-AFM coupling in Mn sublattices caused by progressive decrease of JT distortion. Furthermore, the possibility of having magnetic interactions between the Mn^{3+} and Cr^{3+} ions, probably FM in nature, cannot be ignored. Such Mn^{3+} - Cr^{3+} FM coupling has been reported previously in other Mn-Cr systems like $\text{TbMn}_{1-x}\text{Cr}_x\text{O}_3$ [26], $\text{LaMn}_{1-x}\text{Cr}_x\text{O}_3$ [57–59] and $\text{YMn}_{1-x}\text{Cr}_x\text{O}_3$ [60] systems. The interaction between two Cr^{3+} moments may be ignored in this doping regime because of low Cr concentration. In GdCrO_3 , Cr^{3+} ions have $t^3 e^0$ cubic-field d -electron configurations, which leads to an isotropic t^3 -O- t^3 AFM interactions resulting in canted G -type ordering ($G_x F_z$ in Bertaut's notation) in Cr sublattices below 169 K. The detailed magnetic interactions in GdCrO_3 is reported elsewhere [15]. In Cr-rich compositions, Cr^{3+} - Cr^{3+} interactions dominate and thus have similar behavior to that of GdCrO_3 having a G -type magnetic structure. The canted spin structures in these systems is a direct consequence of antisymmetric Dzyaloshinskii-Moriya (DM) interaction [$D \cdot (\vec{S}_i \times \vec{S}_j)$] [61]. Notably, FCC magnetization curves for $x = 0$ and 0.25 compositions show positive magnetization in the entire temperature region. However, one sees a magnetization reversal effect for all other compositions ($x = 0.5, 0.75$, and 1.0), suggesting the strengthening of AFM coupling between Gd and M sublattices with increasing Cr content. This magnetization reversal as a function of temperature above a critical Cr concentration suggests that there is a strong correlation between the structural distortion and magnetic coupling.

To understand the structural ordering of and magnetic coupling between transition-metal ions and their moments in $\text{GdMn}_{1-x}\text{Cr}_x\text{O}_3$ (for $x = 0.25, 0.5$, and 0.75), the total energy was calculated (within the framework of GGA including Hubbard U) for various possible arrangements of Mn^{3+} and Cr^{3+} ions and for various possible spin configurations. It is reported in $\text{TbMn}_{0.5}\text{Cr}_{0.5}\text{O}_3$ that the results of GGA + U are not significantly different from those obtained including

TABLE I. Calculated relative energies (E , in meV/unit cell) of various magnetic structures of $\text{GdMn}_{0.5}\text{Cr}_{0.5}\text{O}_3$. The unit cell contains two Mn and two Cr spins. The energies of the FM phase with layer-by-layer arrangements along c axis [two Mn (Cr) on the ab plane] is used as the reference energy. Subscripts M and C represent Mn and Cr ions, respectively.

Magnetic structure	C \uparrow C \uparrow	C \uparrow C \downarrow	C \downarrow C \downarrow	C \uparrow C \downarrow	C \uparrow C \downarrow
E	0	-16.15	12.25	131.02	125.33
Magnetic structure	M \uparrow C \uparrow	M \uparrow C \downarrow	M \downarrow C \uparrow	M \downarrow C \downarrow	M \uparrow M \downarrow
E	354.87	332.98	420.76	421.31	
Magnetic structure	M \uparrow C \uparrow	M \uparrow C \uparrow	M \uparrow C \uparrow	M \uparrow C \uparrow	M \uparrow C \uparrow
E	321.31	306.16	343.92	372.3	

spin-orbit coupling (SOC), i.e., GGA+ U +SOC [62]. Therefore, we have not included SOC in the present calculations.

For the $\text{GdMn}_{0.5}\text{Cr}_{0.5}\text{O}_3$ case, we found that the structure with alternate layers of Mn^{3+} and Cr^{3+} ions along the c axis is the one with the lowest energy, independent of the magnetic ordering (the top row entries of Table I). This ordering of the Mn^{3+} and Cr^{3+} ions is found to be the same as in $\text{LaMn}_{0.5}\text{Cr}_{0.5}\text{O}_3$ [63], but different from what was found in $\text{TbMn}_{0.5}\text{Cr}_{0.5}\text{O}_3$ [62], where Mn^{3+} and Cr^{3+} ions alternate along a and c directions. The ordering of the ions can be physically understood by realizing that this arrangement reduces the competing JT distortion energy compared to the situation when Mn^{3+} and Cr^{3+} ions are randomly distributed. Also, the different orderings seen in Tb (f^9) and Gd (f^7) or La (f^0) compounds suggest that orbital anisotropy of the rare earth ions can be important in local structural arrangement and long-range ordering of ions.

To understand the ground-state magnetic structure, we looked at different magnetic orderings as given in Table I. The lowest energy magnetic configuration is alternate planes of FM Mn^{3+} and AFM Cr^{3+} ions. This spin order is also found to be the lowest energy configuration in the case of $\text{LaMn}_{0.5}\text{Cr}_{0.5}\text{O}_3$ [63]. FM order in the basal (ab) plane is also found in GdMnO_3 . Switching the AFM Cr planes to FM Cr planes, keeping the Mn planes FM, increases the energy by ~ 16 meV/MUC (per unit cell containing four TM ions which we will refer to as magnetic unit cell, MUC), whereas changing the Mn planes from FM to AFM increases the energy by ~ 140 meV/MUC. This clearly suggests the FM coupling between the Mn spins in the basal plane is the dominant magnetic coupling in $\text{GdMn}_{0.5}\text{Cr}_{0.5}\text{O}_3$. We have also investigated the effect of local domain formation by Mn and Cr atoms on the magnetic properties within our computational capacity. For this purpose, we constructed a $2 \times 1 \times 1$ supercell which contains four of each Mn and Cr atoms. These atoms were arranged in clusters of three or four Mn(Cr) atoms together. We then made different magnetic configurations by changing the spin orientation of these atoms for intracusters as well as interclusters. The total energies obtained for such configurations are all higher in energy than the above predicted ground state. The theoretical results indicating the ordering of Mn and Cr ions are in agreement with our XRD results. To deeply understand the magnetic structures, we propose below an effective spin Hamiltonian (SH) to estimate the strengths of the different exchange couplings.

In constructing an effective SH to understand the spin-dependent energetics of $\text{GdMn}_{0.5}\text{Cr}_{0.5}\text{O}_3$ only Mn^{3+} and Cr^{3+} spins were considered, since Gd^{3+} spins were not included in the total energy calculations. The unit cell used in the calculation of the energies for different Mn and Cr arrangements and different spin orientations consists of 20 atoms, $\text{Gd}_4\text{Mn}_2\text{Cr}_2\text{O}_{12}$, consisting of two Mn and two Cr ions. The unit cell then consists of four magnetic atoms I-IV; I and II are in one basal plane representing the Cr atoms and III and IV are in the other basal plane representing the Mn atoms as shown schematically in Fig. 7. The structure in the figure is denoted as (Cr \uparrow , Cr \downarrow)(Mn \uparrow , Mn \uparrow), which is the lowest energy atomic structure obtained from the calculations.

The SH for the system is given by

$$H_{\text{spin}} = -J_1 \sum_{\langle ij \rangle l} \vec{S}_{il}^{\text{Mn}} \cdot \vec{S}_{jl}^{\text{Mn}} - J_2 \sum_{\langle ij \rangle l} \vec{S}_{il}^{\text{Cr}} \cdot \vec{S}_{jl}^{\text{Cr}} - J_3 \sum_{\langle ll' \rangle l} \vec{S}_{il}^{\text{Mn}} \cdot \vec{S}_{il'}^{\text{Cr}} + \Delta \quad (1)$$

where i, j indicate lattice sites in the basal (ab) plane and l indicates different layers along the c axis. The number of

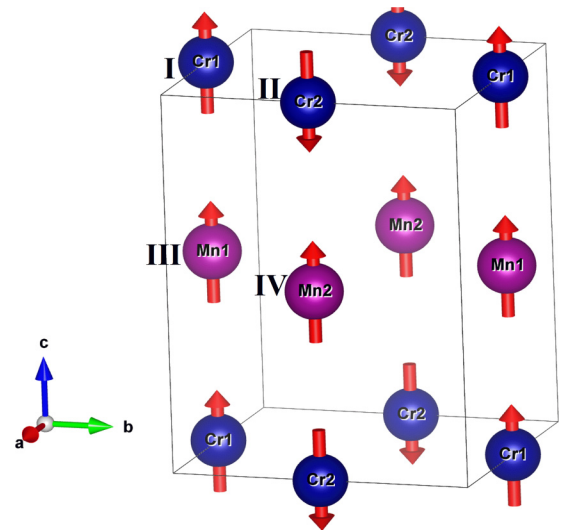


FIG. 7. The calculated most stable magnetic structures in one unit cell for $\text{GdMn}_{0.5}\text{Cr}_{0.5}\text{O}_3$. Only the transition-metal ions Mn and Cr are shown. The ions labeled as I-IV are the nonequivalent atoms in the unit cell, denoted as (C \uparrow , C \downarrow)(M \uparrow , M \uparrow) in Table I.

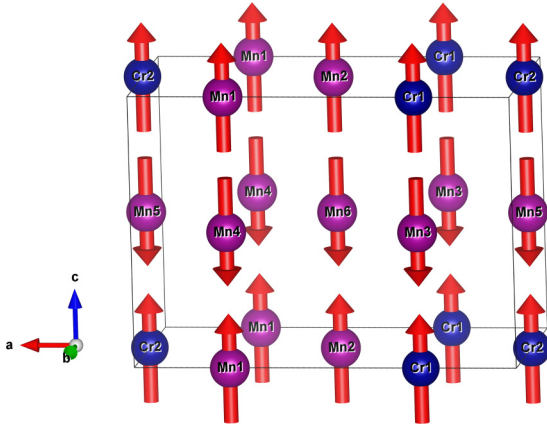


FIG. 8. The calculated most stable structure (atomic and magnetic) with lowest energy for $\text{GdMn}_{0.75}\text{Cr}_{0.25}\text{O}_3$. Only the transition-metal ions Mn and Cr are shown.

Mn–Mn bonds, Cr–Cr bonds, and Mn–Cr bonds per unit cell are four each, as presented in Fig. 8. There are four parameters in the SH which were estimated using calculated DFT energies for different spin configurations with layer-by-layer arrangements of Mn and Cr along the c axis (see Table I, first row). Here $S^{\text{Mn}} = 2$; $S^{\text{Cr}} = 3/2$. In the mean-field approximation, energy/unit-cell (in meV/unit cell) for four different spin configurations are given below. Energy for a fifth configuration can be predicted within a SH model and compared with DFT energy:

$$E_{\text{I}} = -16J_1 - 9J_2 - 12J_3 + \Delta = 0, \quad (2)$$

$$E_{\text{II}} = -16J_1 + 9J_2 + \Delta = -16.15, \quad (3)$$

$$E_{\text{III}} = -16J_1 - 9J_2 + 12J_3 + \Delta = +12.25, \quad (4)$$

$$E_{\text{IV}} = +16J_1 + 9J_2 + 12J_3 + \Delta = +131.02, \quad (5)$$

$$E_{\text{V}} = +16J_1 + 9J_2 - 12J_3 + \Delta. \quad (6)$$

Equations 2–5 can be solved to give: $J_1 = J^{\text{Mn–Mn}} = 4.39$ meV (FM), $J_2 = J^{\text{Cr–Cr}} = -1.26$ meV (AFM), $J_3 = J^{\text{Mn–Cr}} = 0.55$ meV (FM) and $\Delta = 65.48$ meV. Using these parameters, $E_{\text{V}} = 117.78$ meV can be predicted, whereas the calculated DFT energy is 125.33 meV. Looking at the calculated exchange parameters, we observe that the coupling between Mn spins is FM and strong, similar to the parent manganite, i.e., GdMnO_3 . The coupling between Cr spins is AFM, again similar to the parent compound GdCrO_3 . The cross coupling between Mn and Cr spin is FM and weak. It is possible that the small magnitude of $J^{\text{Mn–Cr}}$ results from a near cancellation between two competing contributions, one the usual AFM superexchange and the other FM double exchange.

Different atomic and magnetic structures were also investigated for $x = 0.25$ composition and the lowest energy configuration obtained is shown in Fig. 8. The unit cell consists of alternate layers of Mn^{3+} ions and mixed (50%–50%) Mn^{3+} – Cr^{3+} ions. In contrast, the structure with Cr^{3+} ions occupying every layer was higher in energy by ~ 0.5 eV. The lowest energy structure in the mixed plane consists of alternate double chains of both Mn^{3+} and Cr^{3+} ions along the b axis. The coupling between Mn^{3+} and Cr^{3+} is FM, which is seen

in the basal plane. However, the NN Cr^{3+} and Mn^{3+} spins along the c axis are antiparallel due to the dominance of strong intraplanar FM exchange between the Mn^{3+} spins and reasonably strong NN coupling between the Mn^{3+} spins along the c axis. Ramos *et al.* [59] also suggested from their XAS and x-ray magnetic circular dichroism studies in $\text{LaMn}_{1-x}\text{Cr}_x\text{O}_3$; $0 \leq x \leq 0.15$ that the possibility of a FM double exchange between Mn^{3+} – Cr^{3+} ions within the ab plane, but with an antiparallel alignment of the magnetic component along the c axis. This indicates that complex orbital mixing plays a key role in emergence of ferromagnetism in the compound.

Next we discuss the case $x = 0.75$ composition. The unit cell here has three Cr and one Mn atoms. The system consists of alternate ab planes of pure Cr ions and 50%–50% mixture of Mn and Cr ions. In the Cr-rich compositions, one would expect the dominant magnetic coupling is AFM superexchange between the half-filled t_{2g} orbitals of Cr^{3+} ions. We calculated total energy for different magnetic configurations. As expected, the lowest energy configuration has AFM Cr^{3+} – Cr^{3+} interactions along with a FM Cr^{3+} – Mn^{3+} interactions (no Mn^{3+} – Mn^{3+} coupling) (see Fig. S2 (a) in the Supplemental Material [32]). Permuting various in-plane and out-of-plane Cr^{3+} – Mn^{3+} coupling to AM and/or AFM arrangements while keeping intact the in-plane AFM Cr^{3+} – Cr^{3+} interactions, we found that all such magnetic configurations including the ground state are very close to each other on energy scale (≤ 12 meV) (see Fig. S2 in the Supplemental Material [32]). The reason behind this could be the strongly dominating in-plane AFM superexchange background between Cr^{3+} – Cr^{3+} pairs, which leaves little room for any other weaker magnetic coupling to manifest itself in terms of contribution to the total energy. We also tried supercell calculations to make perfect A-, C-, and G-type magnetic configurations but we could not converge to these desired magnetic structures.

The variation of the remnant magnetization (M_r) at 10 K with compositions (x) for $\text{GdMn}_{1-x}\text{Cr}_x\text{O}_3$ and their corresponding M – H loops are shown in Figs. 9(a) and 9(b), respectively. M_r shows a nonmonotonic variation with composition: Initially, it increases with increasing Cr concentration (x) and reaches a maximum value for $x \sim 0.3$. Beyond $x \sim 0.3$, M_r starts decreasing for increasing x followed by no distinct variation beyond $x \sim 0.7$. As discussed previously, magnetic behavior in the solid solution is a combination of variety of magnetic interactions such as symmetric exchange interactions (FM and AFM type) and antisymmetric DM interaction coupled to octahedral tilting. The DM interaction is directly proportional to the perpendicular displacement of oxygen in the M – O – M chain, which, in turn, depends on the tilt angles [64,65]. It is evident from Raman spectroscopy data that there is hardly any change of tilt angles throughout the series, suggesting that the contributions from canted ferromagnetism (DM interaction) remains almost constant throughout the series. Thus, the increase of M_r up to $x \sim 0.3$ suggests an increase of NN-FM coupling as compared to NNN-AFM coupling caused by the progressive decrease of JT-orbital ordering and incorporation of Mn^{3+} – Cr^{3+} FM interactions as discussed earlier. Beyond $x \sim 0.3$, a ferrimagnetic-type structure arises due to the incorporation of AFM Cr^{3+} – Cr^{3+} interactions, thus resulting in decrease of M_r . In Cr-rich compositions ($x \geq 0.7$), AFM

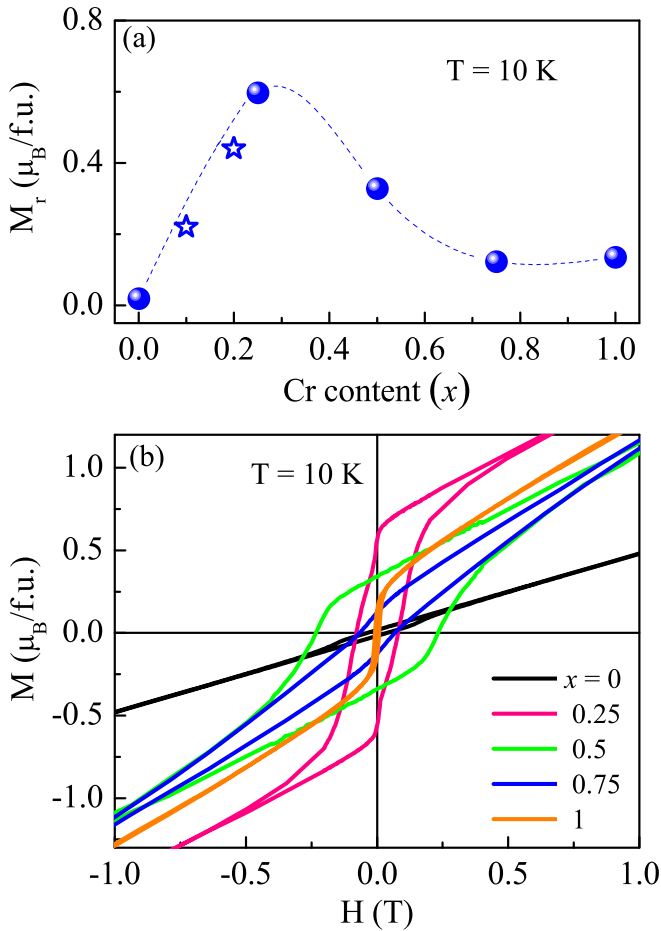


FIG. 9. (a) Variation of remnant magnetization (M_r) at 10 K with compositions (x). Stars (*) represent the results extracted from Ref. [21]. (b) Enlarged view of M - H loops measured at 10 K of the solid solutions for $x = 0, 0.25, 0.5, 0.75$, and 1.

Cr^{3+} - Cr^{3+} interactions are more dominating, resulting in no further change in M_r .

IV. CONCLUSION

The structural, electronic, and magnetic properties of $\text{GdMn}_{1-x}\text{Cr}_x\text{O}_3$ were studied. The Rietveld refinement of

XRD pattern shows that monoclinic $P2_1/b$ structure with alternate stacking of Mn and Cr layers along [001] direction is more reliable for $\text{GdMn}_{0.5}\text{Cr}_{0.5}\text{O}_3$. In structural investigations, it was found that the JT distortion characteristic to Mn^{3+} results in bond anisotropy and effective orbital ordering for $x \leq 0.35$. A gradual variation of electronic states with doping is also clearly seen in O-K edge x-ray absorption spectra. The temperature dependence of magnetization under the FCC mode shows sign reversal effects for $x \geq 0.35$, whereas magnetization does not change signs in the JT-active region. The change in magnetic polarity at the critical concentration coinciding with JT crossover implies a complex interplay of magnetic interaction and structural distortion. The nonmonotonic variation of remnant magnetization can be understood in terms of doping-induced modification of symmetric magnetic interactions (FM/AFM type). DFT calculations using GGA + U -type exchange correlation potential find that the system with $x = 0.5$ consists of alternate FM Mn layers and AFM Cr layers. The strength of the FM exchange interaction between NN Mn spins is stronger than the NN Cr AFM exchange. The exchange interaction between NN Mn and Cr is quite small but ferromagnetic. This is distinctly different from the magnetic structures of both end members GdMnO_3 and GdCrO_3 . For $x = 0.25$, there exist alternate planes of Mn and Mn-Cr; the Mn-Cr layers consist of alternate Mn-Mn-Cr-Cr chains along the b axis. Both planes are FM but are antiferromagnetically oriented to each other. For $x = 0.75$, there is an alternate arrangement of Cr and Cr-Mn layers. The dominant interaction is an AFM type between Cr ions within the ab plane along with FM coupling between Cr-Mn ions.

ACKNOWLEDGMENTS

B.R. would like to thank Prof. P. V. Satyam, IOP, Bhubaneswar, India for computational facilities. S.K.P. gratefully acknowledges the computational support provided by Professor Ji Feng for the last few calculations. The authors acknowledge the financial support given for the measurements at Elettra Synchrotron under Indo-Italian (DST- ICTP) Cooperation Program.

- [1] R. H. Mitchell, *Perovskites: Modern and Ancient* (Almaz Press, Thunder Bay, Ontario, 2002).
- [2] A. Glazer, *Acta Cryst.* **28**, 3384 (1972).
- [3] A. Glazer, *Acta Cryst.* **31**, 756 (1975).
- [4] J.-S. Zhou and J. B. Goodenough, *Phys. Rev. Lett.* **96**, 247202 (2006).
- [5] C. N. R. Rao and B. Raveau, *Colossal Magnetoresistance, Charge Ordering and Related Properties of Manganese Oxides* (World Scientific Publishing Co Pte Ltd, Singapore, 1998).
- [6] S. Mori, T. Katsufuji, N. Yamamoto, C. H. Chen, and S. W. Cheong, *Phys. Rev. B* **59**, 13573 (1999).
- [7] J. van den Brink, G. Khaliullin, and D. Khomskii, *Phys. Rev. Lett.* **83**, 5118 (1999).
- [8] T. Asaka, S. Yamada, S. Tsutsumi, C. Tsuruta, K. Kimoto, T. Arima, and Y. Matsui, *Phys. Rev. Lett.* **88**, 097201 (2002).
- [9] H. Kawano, R. Kajimoto, H. Yoshizawa, Y. Tomioka, H. Kuwahara, and Y. Tokura, *Phys. Rev. Lett.* **78**, 4253 (1997).
- [10] N. Fukumoto, S. Mori, N. Yamamoto, Y. Moritomo, T. Katsufuji, C. H. Chen, and S. W. Cheong, *Phys. Rev. B* **60**, 12963 (1999).
- [11] M. Mochizuki and N. Furukawa, *Phys. Rev. B* **80**, 134416 (2009).
- [12] S.-W. Cheong and M. Mostovoy, *Nat. Mater.* **6**, 13 (2007).
- [13] B. Rajeswaran, D. I. Khomskii, A. K. Zvezdin, C. N. R. Rao, and A. Sundaresan, *Phys. Rev. B* **86**, 214409 (2012).
- [14] S. Mahana, B. Rakshit, R. Basu, S. Dhara, B. Joseph, U. Manju, S. D. Mahanti, and D. Topwal, *Phys. Rev. B* **96**, 104106 (2017).

- [15] S. Mahana, U. Manju, and D. Topwal, in *AIP Conference Proceedings*, Vol. 1832 (AIP Publishing LLC, Melville, NY, USA, 2017), p. 130046.
- [16] Y. Cao, S. Cao, W. Ren, Z. Feng, S. Yuan, B. Kang, B. Lu, and J. Zhang, *Appl. Phys. Lett.* **104**, 232405 (2014).
- [17] M. El Amrani, M. Zaghrioui, V. T. Phuoc, F. Gervais, and N. E. Massa, *J. Magn. Magn. Mater.* **361**, 1 (2014).
- [18] S. Mahana, U. Manju, and D. Topwal, *J. Phys. D: Appl. Phys.* **50**, 035002 (2017).
- [19] T. Kimura, G. Lawes, T. Goto, Y. Tokura, and A. P. Ramirez, *Phys. Rev. B* **71**, 224425 (2005).
- [20] J. A. Moreira, A. Almeida, M. Chaves, J. Kreisel, J. Oliveira, F. Carpinteiro, and P. Tavares, *J. Phys.: Condens. Matter* **24**, 436002 (2012).
- [21] A. Modi and N. Gaur, *J. Alloys Compounds* **644**, 575 (2015).
- [22] F.-K. Chiang, M.-W. Chu, F. C. Chou, H. T. Jeng, H. S. Sheu, F. R. Chen, and C. H. Chen, *Phys. Rev. B* **83**, 245105 (2011).
- [23] Z. Long and W. Xiao-Shan, *Chin. Phys. B* **22**, 107806 (2013).
- [24] Y. Fang, Y. Yang, X. Liu, J. Kang, L. Hao, X. Chen, L. Xie, G. Sun, V. Chandragiri, C.-W. Wang *et al.*, *Sci. Rep.* **6**, 33448 (2016).
- [25] Y.-H. Huang, M. Karppinen, N. Imamura, H. Yamauchi, and J. B. Goodenough, *Phys. Rev. B* **76**, 174405 (2007).
- [26] M. Staruch and M. Jain, *J. Phys.: Condens. Matter* **26**, 046005 (2014).
- [27] J. P. Perdew, A. Ruzsinszky, G. I. Csonka, O. A. Vydrov, G. E. Scuseria, L. A. Constantin, X. Zhou, and K. Burke, *Phys. Rev. Lett.* **100**, 136406 (2008).
- [28] G. Kresse and D. Joubert, *Phys. Rev. B* **59**, 1758 (1999).
- [29] G. Kresse and J. Furthmüller, *Phys. Rev. B* **54**, 11169 (1996).
- [30] H. J. Monkhorst and J. D. Pack, *Phys. Rev. B* **13**, 5188 (1976).
- [31] K. Yamauchi, F. Freimuth, S. Blügel, and S. Picozzi, *Phys. Rev. B* **78**, 014403 (2008).
- [32] See Supplemental Material at <http://link.aps.org/supplemental/10.1103/PhysRevB.102.245120> for refinement results of powder XRD for GdMn_{0.5}Cr_{0.5}O₃, calculated degenerate magnetic structures of GdMn_{0.25}Cr_{0.75}O₃, and refined atomic parameters of all compositions.
- [33] L. Hao, L. Yang, M.-H. Lee, T.-H. Lin, Z. Zhang, X. Xie, and H. Zhu, *J. Alloys Compd.* **601**, 14 (2014).
- [34] J.-S. Zhou, J. A. Alonso, V. Pomjakushin, J. B. Goodenough, Y. Ren, J.-Q. Yan, and J.-G. Cheng, *Phys. Rev. B* **81**, 214115 (2010).
- [35] J.-S. Zhou and J. B. Goodenough, *Phys. Rev. B* **77**, 132104 (2008).
- [36] M. Tachibana, T. Shimoyama, H. Kawaji, T. Atake, and E. Takayama-Muromachi, *Phys. Rev. B* **75**, 144425 (2007).
- [37] J. Kanamori, *J. Appl. Phys.* **31**, S14 (1960).
- [38] J.-S. Zhou and J. B. Goodenough, *Phys. Rev. B* **77**, 172409 (2008).
- [39] M. N. Iliev, M. V. Abrashev, J. Laverdiere, S. Jandl, M. M. Gospodinov, Y.-Q. Wang, and Y.-Y. Sun, *Phys. Rev. B* **73**, 064302 (2006).
- [40] N. D. Todorov, M. V. Abrashev, V. G. Ivanov, G. G. Tsutsumanova, V. Marinova, Y.-Q. Wang, and M. N. Iliev, *Phys. Rev. B* **83**, 224303 (2011).
- [41] M. N. Iliev, A. P. Litvinchuk, V. G. Hadjiev, Y.-Q. Wang, J. Cmaidalka, R.-L. Meng, Y.-Y. Sun, N. Kolev, and M. Abrashev, *Phys. Rev. B* **74**, 214301 (2006).
- [42] M. V. Abrashev, J. Bäckström, L. Börjesson, V. N. Popov, R. A. Chakalov, N. Kolev, R.-L. Meng, and M. Iliev, *Phys. Rev. B* **65**, 184301 (2002).
- [43] M. N. Iliev, V. G. Hadjiev, A. P. Litvinchuk, F. Yen, Y.-Q. Wang, Y. Y. Sun, S. Jandl, J. Laverdiere, V. N. Popov, and M. M. Gospodinov, *Phys. Rev. B* **75**, 064303 (2007).
- [44] M. N. Iliev, M. V. Abrashev, V. N. Popov, and V. G. Hadjiev, *Phys. Rev. B* **67**, 212301 (2003).
- [45] N. N. Kovaleva, O. E. Kusmartseva, K. Kugel, A. Maksimov, D. Nuzhnyy, A. Balbashov, E. Demikhov, A. Dejneka, V. Trepakov, F. Kusmartsev *et al.*, *J. Phys.: Condens. Matter* **25**, 155602 (2013).
- [46] Y. Zhao, D. J. Weidner, J. B. Parise, and D. E. Cox, *Phys. Earth Planet. Inter.* **76**, 17 (1993).
- [47] M. C. Weber, J. Kreisel, P. A. Thomas, M. Newton, K. Sardar, and R. I. Walton, *Phys. Rev. B* **85**, 054303 (2012).
- [48] L. M. Daniels, M. C. Weber, M. R. Lees, M. Guennou, R. J. Kashtiban, J. Sloan, J. Kreisel, and R. I. Walton, *Inorg. Chem.* **52**, 12161 (2013).
- [49] L. Martín-Carrón, A. De Andres, M. J. Martínez-Lope, M. T. Casais, and J. A. Alonso, *Phys. Rev. B* **66**, 174303 (2002).
- [50] J. Chen, J. Lee, C. Chen, T. Chou, K. Lu, S. Haw, K. Liang, C. Chen, H. Jeng, S. Huang *et al.*, *Appl. Phys. Lett.* **94**, 044105 (2009).
- [51] J. M. Chen, Z. Hu, H. T. Jeng, Y.Y. Chin, J. M. Lee, S.W. Huang, K.T. Lu, C.K. Chen, S. C. Haw, T. L. Chou, H. J. Lin, C. C. Shen, R. S. Liu, A. Tanaka, L. H. Tjeng, and C. T. Chen, *Phys. Rev. B* **81**, 201102(R) (2010).
- [52] S. Bukhari and J. Ahmad, *Acta Phys. Pol. A* **129**, 43 (2016).
- [53] G. Kotnana and S. N. Jammalamadaka, *J. Appl. Phys.* **118**, 124101 (2015).
- [54] P. Gupta and P. Poddar, *RSC Adv.* **6**, 82014 (2016).
- [55] M. Richter, *J. Phys. D* **31**, 1017 (1998).
- [56] A. Stroppa, M. Marsman, G. Kresse, and S. Picozzi, *New J. Phys.* **12**, 093026 (2010).
- [57] U. Bents, *Phys. Rev.* **106**, 225 (1957).
- [58] L. Morales, R. Allub, B. Alascio, A. Butera, and A. Caneiro, *Phys. Rev. B* **72**, 132413 (2005).
- [59] A. Y. Ramos, H. C. N. Tolentino, M. M. Soares, S. Grenier, O. Bunau, Y. Joly, F. Baudelet, F. Wilhelm, A. Rogalev, R. A. Souza, N. M. Souza-Neto, O. Proux, D. Testemale, and A. Caneiro, *Phys. Rev. B* **87**, 220404(R) (2013).
- [60] S. Li, T. Wang, H. Han, X. Wang, H. Li, J. Liu, and J. Liu, *J. Phys. D* **45**, 055003 (2012).
- [61] T. Moriya, *Phys. Rev.* **120**, 91 (1960).
- [62] M. Staruch, V. Sharma, C. dela Cruz, R. Ramprasad, and M. Jain, *J. Appl. Phys.* **116**, 033919 (2014).
- [63] Z. Yang, L. Ye, and X. Xie, *J. Phys.: Condens. Matter* **12**, 2737 (2000).
- [64] L. Bellaiche, Z. Gui, and I. A. Kornev, *J. Phys.: Condens. Matter* **24**, 312201 (2012).
- [65] A. Singh, A. Senyshyn, H. Fuess, S. J. Kennedy, and D. Pandey, *Phys. Rev. B* **89**, 024108 (2014).